Journal of The Electrochemical Society, **158** (10) A1123-A1135 (2011)
0013-4651/2011/158(10)/A1123/13/$28.00 © The Electrochemical Society

Aging of a Commercial Graphite/$LiFePO_4$ Cell

M. Safari[a,b,*] **and C. Delacourt**[a,**,z]

[a]*Laboratoire de Reactivité et Chimie des Solides, UMR CNRS 6007, Université de Picardie Jules Verne, 80039 Amiens, France*
[b]*Renault Research Department, 78288 Guyancourt, France*

The aging behavior of a commercial 2.3 Ah graphite/LFP cell during a year of cycling or storage at either 25 or 45°C is investigated. The performance decline of the cells during the aging period is monitored by non-destructive electrochemical techniques and is discussed in detail. An in-depth analysis of the aging results reveals that aging manifests itself more in terms of capacity loss rather than in terms of impedance increase, regardless of the cycling or storage conditions and of the temperature. The capacity fade is larger at 45°C than at 25°C, regardless of the cycling or storage conditions, and at a same temperature, cycling conditions are always more detrimental to capacity fade than storage conditions. The loss of cyclable lithium is identified as the main source of capacity fade in all cases, and for the cells aged at 45°C, a partial loss of graphite active material is suspected as well towards the end of the aging period.
 [DOI: 10.1149/1.3614529]

Manuscript submitted May 23, 2011; revised manuscript received June 28, 2011. Published August 12, 2011.

Since the introduction of $LiFePO_4$ (LFP) electrode to the lithium-ion battery community in 1997 by Padhi et al.,[1] there has been a lot of effort to commercialize LFP-based cells that meet energy and power demands of current automotive industry. Commercial graphite/LFP cells are now on the market and compete with others like $LiMn_2O_4$ or $LiNi_{1/3}Co_{1/3}Mn_{1/3}O_2$ -based cells. Beside energy and power density as well as safety, the cell longevity is of major concern for many applications such as electric transportation where lifetime up to 10 years is demanded.[2] Hence, an evaluation of the performance decline of a cell subject to operating conditions typical of a defined application is necessary. Aging studies on graphite/LFP cells were initiated by Striebel et al.[3] in 2003. Aging of 1.6 mAh graphite/LFP pouch cells under cycling and storage at 25°C over short periods was reported. They showed similar rates of capacity fade for cells stored at open circuit at nearly 100% state of charge (SOC) and others cycled at C/2. Postmortem analyses revealed that the LFP electrode had not undergone any change while the graphite one had lost part of its original capacity along with less defined potential plateaus. However, the major performance fade of the cells was reported to arise from side reactions that consume cyclable lithium and increase the interfacial resistance of the anode. Subsequent papers by Shim et al.,[4] and Zaghib et al.,[5] proposed the same aging mechanism for cycle aging of the cell at 25°C. Later on, Striebel et al.,[6] studied the cell aging under cycling at 25°C over 400 cycles at C/2 for two different setups involving either $LiPF_6$ or LiBOB as the lithium salt in the electrolyte formulation. They reported two times more capacity loss for the case with $LiPF_6$ as the lithium salt. Having confirmed the presence of iron at the graphite electrode using transmission electron microscopy and Raman spectroscopy, they proposed that the solid electrolyte interphase (SEI) is formed continuously on the surface of graphite particles over cycling by the catalytic effect of dissolved iron from LFP electrode while maintaining either a steady thickness or a very high conductivity. At the same time, Amine et al.[7] confirmed iron dissolution from aging experiments on 110 mAh prismatic MCMB/LFP cells resulting in 60% capacity loss over 100 cycles at C/3 and 55°C. Following studies mainly focused on iron dissolution from LFP electrodes and its contribution to the cell aging. Zaghib et al.[8] showed that iron dissolution is caused by Fe impurities in the LFP electrodes, as illustrated by the good capacity retention of a 160 mAh graphite/LFP cell with an optimized LFP electrode after 200 cycles at 1C and 60°C. In 2007, Koltypin et al.[9] reported a complete study on iron dissolution from LFP electrodes in different electrolytic solutions. By performing FTIR, XPS, and Raman spectroscopy analyses, they proposed that in the presence of H_3O^+ ions in the electrolyte, an ion exchange between H^+ and Fe^{2+} ions develop surface films on LFP electrode which are rich in LiF and phosphorous compounds. Moreover, they confirmed that the alkyl-carbonate surface films grow even in the absence of iron dissolution in alkyl-based electrolytes, in a similar way to $LiNiO_2$ and $LiCoO_2$ electrodes aged at elevated temperatures. The same authors, in a parallel work, showed that the LFP electrodes synthesized from a sol-gel route were the most stable against iron dissolution due to the higher iron phosphide content on the LFP surface, whereas the samples synthesized by a hydrothermal method showed the highest rates of iron dissolution.[10] In 2009, Dubarry et al.[11] were the first to report on aging of commercial graphite/LFP cells (18,650 cylindrical cell of 1.45 Ah) at 25°C under cycling. In order to pinpoint the cause of aging, they combined the differential-capacity analysis and SOC tracing of the cell over 600 cycles. Similar to earlier studies, they concluded that aging mainly results from the formation of a Li-consuming SEI layer at the graphite electrode. Liu et al.[12] recently published a cycle-aging study of a commercial 2.3 Ah graphite/LFP cell at different temperatures, depths of discharge, and C-rates. By introducing a micro-reference electrode to the cell design, they could follow the potential of the graphite electrode during cycling. Differentiation analysis of the discharge profiles as well as in situ reference electrode measurements revealed a loss of cyclable lithium as well as a degradation of the carbon anode. Moreover, atomic absorption spectroscopy and EDX confirmed that iron dissolution does not play a major role in the aging process, which is in line with the negligible increase of the cell resistance over cycling. Later on, the same group proposed that there is a square-root-of-time dependence of capacity loss at different C-rates for this commercial cell.[13]

In spite of a few aging studies on commercial graphite/LFP cells,[11–15] reports on the long-term aging of this chemistry during cycling and more specifically under storage conditions are scarce. Quantifying aging under storage and cycling is a prerequisite for life evaluation of the cell in applications like electric vehicles (EVs), in which most of the battery life is spent under storage. In this study, we present aging results on a commercial 2.3 Ah graphite/LFP cell during a year of cycling or storage at either 25 or 45°C. The performance decline of the cells during the aging period is monitored by non-destructive methods and is discussed in detail.

Experimental

Experiments were conducted on 8 similar commercial 2.3 Ah 26650 graphite/LFP cells. A multichannel battery tester (SBT2050, PEC, Belgium) was used for 1-year cycle aging of the cells, and the electrochemical intermediate characterization tests were performed

* Electrochemical Society Student Member.
** Electrochemical Society Active Member.
z E-mail: charles.delacourt@u-picardie.fr

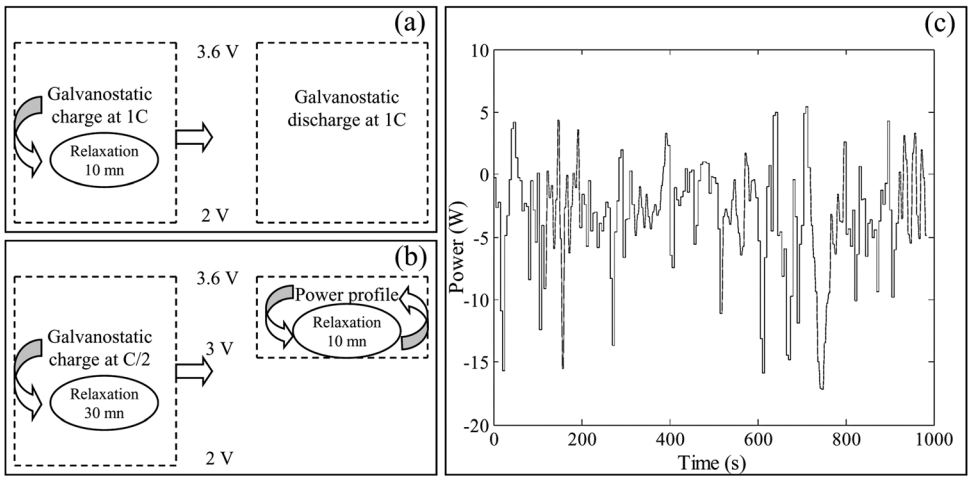

Figure 1. Different cycling profiles used in the aging experiments under cycling. (a) simple cycling (b) complex cycling (c) the elementary power profile used for the discharge part of the complex cycling.

using a multipotentiostat outfitted with a 10 A booster (VMP3, Biologic, France).

The cells were either cycled or stored at two different temperatures, i.e., 25 and 45°C, during a year. Among the four cells under cycling, two of them underwent a conventional $1C_{nom}$ (i.e., 2.3 A) charge/discharge between 2 and 3.6 V with 10 min rest between each consecutive charge and discharge. This cycling protocol is referred to as simple cycling in the following. Beside, a complex current-power profile, more typical of the usage profile of an EV, was used to cycle the other two cells. In this profile, the cell is first charged at $C_{nom}/2$ up to 3.6 V, after which it is left to rest for 30 min and then discharged down to 3 V by the repetition of a power profile lasting for 985 s and followed by a 10 min rest period. The power profile is composed of 38 charging and 159 discharging peaks of 5 s each. The average C-rates corresponding to the charging and discharging power peaks are 0.05 and $0.5C_{nom}$, respectively. Schematics of simple and complex cycling modes are shown in Fig. 1, along with the elementary power profile used for building the complex cycling mode. For the cells under storage, the effect of SOC on aging is studied: two cells are stored at SOC 50% and the other two at SOC 100%.

In order to evaluate the state of health (SOH) of the cells over the course of aging, a series of intermediate electrochemical tests was performed after 1, 3, 6, and 9 months of cycling/storage and at 25°C in a similar way for all cells. First, the cycling or storage was interrupted, the cell temperature was set to 25°C, and the remaining cell capacity was measured using a constant-current/constant-voltage (CCCV) charge/discharge between 2 and 3.6 V, with the condition $|I| < C_{nom}/25$ on the CV segment. A single charge/discharge cycle was used for the cells under cycle aging, whereas three cycles were used for the OCP-stored cells to decipher the reversible and irreversible portions of capacity loss after storage. This measured capacity is then used to update the SOC and C-rate values for the intermediate electrochemical tests described below. The intermediate electrochemical tests consist of charge/discharge rate-capability tests, current pulses at different SOCs (20, 40, 60, and 80%), impedance spectroscopy (EIS) at different SOCs (0, 20, 40, 60, 80, and 100%), and the potentiostatic-intermittent-titration technique (PITT). The rate-capability tests are performed at C-rates ranging from C/10 to 3C by galvanostatic discharge/charge between 2 and 3.6 V. A CCCV protocol is used on both charge and discharge (CV until $|I| < C/25$) to make sure the cell comes back to a fully charged and discharged state, respectively. For current-pulse and impedance tests, the SOC is first adjusted by partially charging or discharging the cell at C/5, after which it is rested for 1 h before measurements are performed. The current-pulse test consists of discharging and charging current peaks at 1, 2, and $4C_{nom}$. The peak duration is 30 s and there is a 10 min rest between every consecutive discharge and charge periods. EIS was performed by perturbing the open-circuit potential with an AC sinusoidal potential of 5 mV amplitude and a frequency ranging from 200 kHz to 10 mHz. The

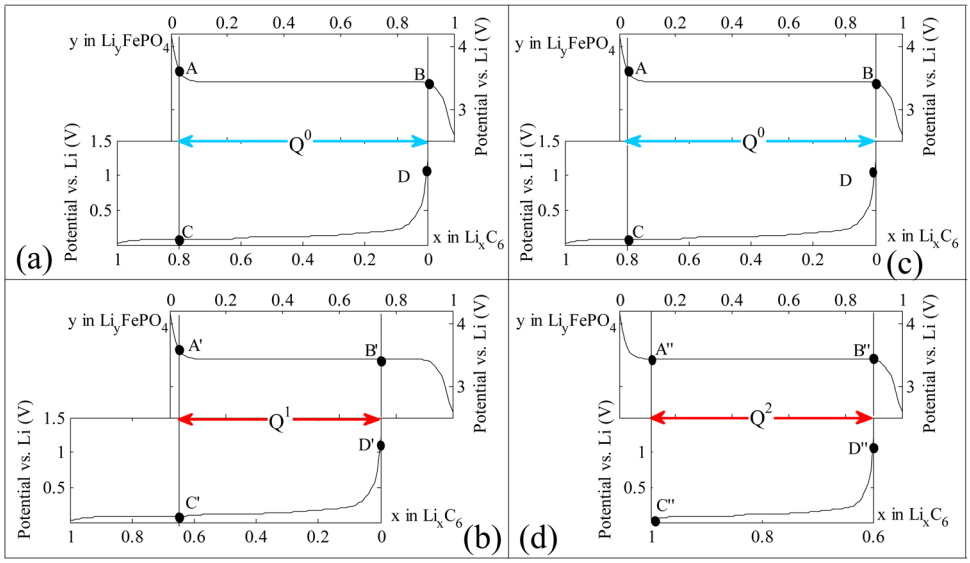

Figure 2. (Color online) Operating stoichiometry window of the graphite/LFP cell defined by the OCP functions of the graphite and LFP electrodes (a, c) before aging (b) after an aging scenario where part of the cyclable lithium was lost during charge or storage of the cell at a completely charged state (d) after an aging scenario where part of the delithiated graphite active material was lost during discharge or storage of the cell at a completely discharged state.

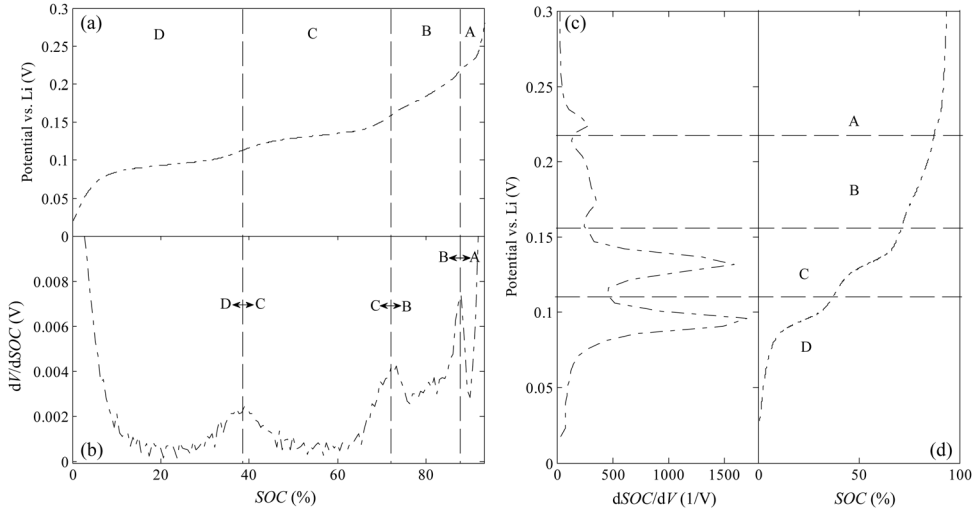

Figure 3. (a) (d) Potential as a function of SOC during galvanostatic charging at C/25 and 25°C of a graphite electrode similar to that in the graphite/LFP cells studied here and the corresponding (b) differential-voltage and (c) differential-capacity graphs that were numerically calculated.

potentiostatic-intermittent-titration technique consisted of a "staircase" potential profile in which the cell potential was increased (decreased) by 10 mV increments between 2 and 3.6 V, and the current decay vs. time was measured at each potential step. Each individual titration was terminated when the absolute current reached a value corresponding to C/25.

Results and Discussion

Aging-analysis framework.—Before presenting the results, the angle from which the aging problem is looked at in the rest of the paper is introduced. Aging phenomena that contribute to decrease the battery lifetime are numerous, and are specific to the cell chemistry.[16–18] They can be either of mechanical or chemical origin. Active-particle isolation from the electrode matrix because of expansion/contraction during cycling is an example of mechanical degradation, while the SEI growth on carbonaceous anodes as a consequence of electrolyte decomposition is an example of chemical degradation. Cell capacity fade may be the result of the loss of cyclable lithium (i.e., increase of the cell imbalance) or of the loss of active materials (e.g., particle isolation, phase transition towards an inactive phase, material decomposition or exfoliation). Additionally, an impedance increase of the cell results in a decrease of its capacity when measured at substantial current density. The change in cyclable-lithium content of the cell is related to an overall balance of the side reactions that occur at both electrodes. For instance, if a side reaction like electrolyte oxidation occurs at the cathode with a lithium-consumption rate identical to that of electrolyte reduction leading to SEI growth at the anode, the cell does not experience a net loss in cyclable lithium; it only results in a self-discharge (i.e., reversible capacity fade) of the cell when OCV-stored, as well as a progressive degradation of the electrolyte. Additionally, the side reactions at both electrodes can be coupled through a shuttle species, i.e., a product of a side reaction at an electrode is the reactant of another side reaction at the other electrode.

A precise theoretical treatment of capacity loss in lithium-ion batteries can be found in Refs. 18 and 19. In Fig. 2, the graphical representation of two different scenarios of capacity loss of a graphite/LFP cell is displayed. Figures 2a and 2c show the initial state of the cell where operating stoichiometry windows are between circles A and B for the LFP electrode and between circles C and D for the graphite electrode. The OCP functions of each electrode and the initial balancing of the cell were taken from Ref. 20 where a mathematical model of the same cell as that studied here was developed. On such a graphical representation, a loss of cyclable lithium manifests itself as a shift in the relative position of the OCP-stoichiometry curves of the electrodes whereas an active-material loss is accounted for by a shrinkage of the OCP-stoichiometry curve of the material.[18,19]

Figure 2b presents a case where part of the cyclable lithium was lost during charging or storage of the cell at a completely charged state. The OCP-stoichiometry graph of the graphite electrode shifts towards the left side and the cell capacity decreases from Q^0 to Q^1 as a result of a smaller stoichiometry window available for cycling. The loss of delithiated graphite active-material while discharging the cell or cell storage at a completely discharged state is shown in Fig. 2d. In this case, the OCP-stoichiometry graph of the graphite electrode shrinks and the cell capacity decreases from Q^0 to Q^2. In both cases presented in Figs. 2b and 2d, the operating stoichiometry window of the cell is changed as a result of aging. x_{max} and y_{max} for graphite and LFP electrodes, respectively, decreased in the case of cyclable-lithium loss (Fig. 2b) whereas the graphite electrode capacity was completely utilized for the case presented in Fig. 2d and y_{min} increased for the LFP electrode.

Drawing the precise picture of aging scenarios like those exemplified in Fig. 2 is not straightforward unless the cell is taken apart and separate electrochemical and structural tests are performed on the

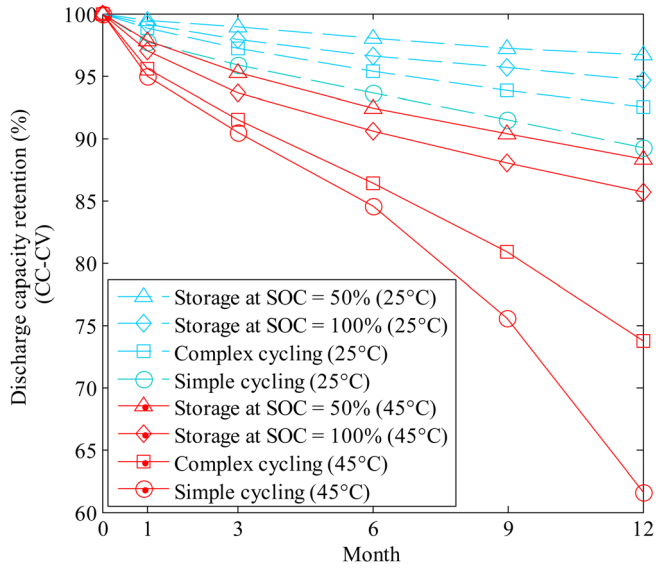

Figure 4. (Color online) Discharge-capacity retention measured in CCCV conditions (CC at C/10, CV before I < C/25) during the intermediate characterization periods at 25°C for 8 graphite/LFP cells under different aging conditions.

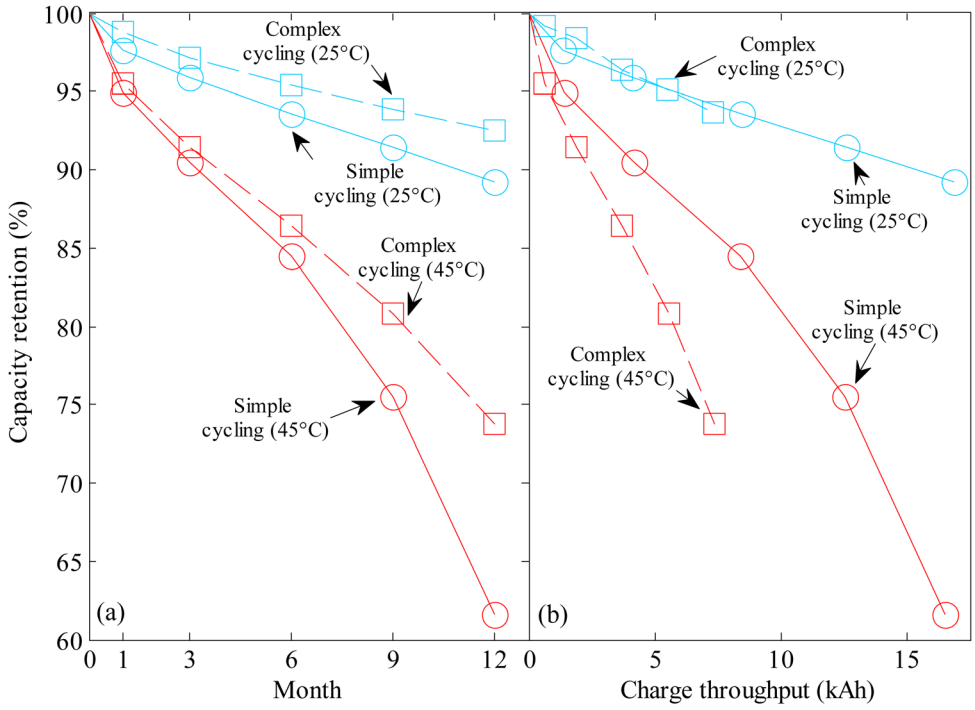

Figure 5. (Color online) Discharge-capacity retention of graphite/LFP cells aged under simple (circle markers) or complex (square markers) modes of cycling (a) as a function of time (b) as a function of charge throughput.

different cell components. However, postmortem analyses do not reveal the complete aging path the cell has went through and only unveils the end-of-life picture of the cell. Here, the possibility of using a mathematical model that can simulate the electrochemical behavior of the cell is very helpful.[21] Postmortem analyses and modeling of the cells studied in this paper will be reported later. Here, the aging results are analyzed and the most likely scenarios are proposed, but still need to be validated based on postmortem studies of the cells.

The capacity-voltage curve of the graphite/LFP cell contains information about both graphite and LFP electrodes but it is not possible to separate the contribution of each electrode. More specifically, the stoichiometry utilization window of each electrode remains unknown. The differential-capacity (dQ/dV) and differential-voltage (dV/dQ) analyses are useful to visualize the phase transitions of the electrodes. These analyses are based on the original work by Thompson[22] where the electrochemical potential spectroscopy was proposed as a new electrochemical measurement technique for studying

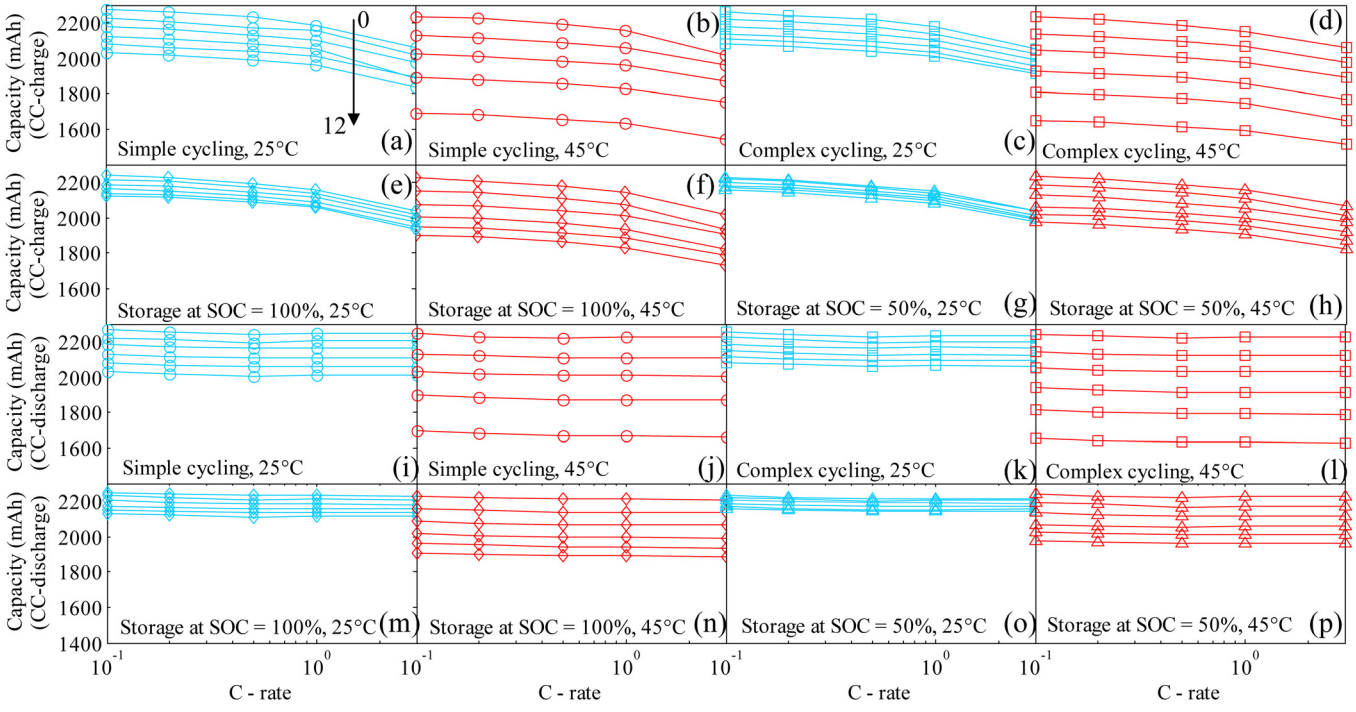

Figure 6. (Color online) Rate capability of the graphite/LFP cells measured during the intermediate characterization periods at 25°C during a year of aging in different conditions. (a) to (h) Rate capability on charge (i) to (p) rate capability on discharge.

electrode materials and was used later on by Bloom et al.[23,24] and Dubarry et al.[25] to study battery aging. A peak in the V - dQ/dV plot features the equilibrium between different electrochemically-active phases in the electrode whereas a peak in the Q - dV/dQ plot locates the transition from one equilibrium to another. In Fig. 3, the SOC - dV/dSOC and V - dSOC$/dV$ graphs of a graphite electrode are presented. These graphs were obtained by numerical differentiation of the C/25 galvanostatic charge of a fully lithiated graphite electrode (Fig. 6a in Ref. 20) taken from a graphite/LFP cell of the same type as those studied here. At least four regions are evident in the V – SOC graphs of Fig. 3, which stem from the staging phenomenon that is a characteristic feature of graphite intercalation compounds.[26] In Fig. 3, the intercalation-deintercalation window of the graphite electrode has been divided in four regions, namely A, B, C, and D. The capacity (ΔSOC) attributed to each region can be calculated either from the surface area under the peaks in the V - dSOC$/dV$ representation or from the distance between two consecutive peaks in the SOC - dV/dSOC plot. The number of peaks in the SOC - dV/dSOC graph is always one less than the peak numbers in the V - dSOC$/dV$ graph and so capacities corresponding to regions D and A are calculated from the peak distances between the origin and the first peak and between the last peak and the total capacity, respectively. As discussed by Bloom et al.[23,24] and Dubarry et al.,[25] any change in the peak position and/or intensity in V - dQ/dV and Q - dV/dQ representations is indicative of aging. The two representations are complementary for aging analysis; Any change of the cell impedance is easily identified from the V - dQ/dV graph whereas it is more straightforward to identify active-material loss and cyclable lithium loss from the Q - dV/dQ representation.

In the graphite/LFP cell, differential-voltage and differential-capacity plots are dominated by the graphite electrode as the LFP electrode operates on a single plateau at 3.43 V vs Li over most of the Li stoichiometry range. Moreover, the previous knowledge on aging of other systems based on the same chemistry suggests that the graphite electrode will probably have a major contribution to the cell aging. The rest of the paper deals with the analysis of the experimental aging data with a special attention to the modifications of the graphite-electrode signature.

Aging results.—The capacity retention of the cells cycled or stored in different conditions over a year are represented in Fig. 4 as a function of time. The cell capacities used to calculate the capacity-retention percentages are from CCCV (CC at C/10 and CV until $|I| <$ C/25) discharge data of the cells during the intermediate characterization periods. The capacity-retention trends presented in this figure are considered to reflect the irreversible capacity loss of the cells as long as the same cutoff potentials are used to cycle the cell. The reported capacity-retention values in Fig. 4 could be lower for galvanostatic cycling of the cell at higher current in the presence of polarization effects. Aging is very sensitive to the temperature at which the cells were aged, as two distinct groups of capacity-retention lines are clearly observed in Fig. 4, with the group of tests at 45°C lying below that at 25°C. The comparison of the cells aged at a same temperature shows that the cells under cycling lose more capacity than those under OCP storage. The capacity-retention lines are almost evenly spaced at 25°C; however, there is a clear separation between the cells aged under cycling and storage at 45°C. Regardless of the aging conditions, there is a nearly linear decrease in capacity of the cells except during the first few months. Moreover, the rate of capacity fade increases for the cells cycled at 45°C from about 6 months, especially for the cell under simple cycling. For the cells stored at the same temperature, more capacity fade is experienced for the cell stored at 100%. Regarding the impact of cycling mode on the cell capacity retention as a function of time, it is perceived from data in Fig. 4 that simple cycling is more detrimental to the battery health. However, the time dependence of the extent of aging is not sufficient to draw some conclusion about the impact of the cycling mode on the aging of cells that were cycled at different C-rates and/or SOC windows, such as simple and complex cycling modes used in this study. As it was described in the'Experimental' section, the average C-rate corresponding to charging and discharging peaks in the elementary power profile of the complex cycling mode are 0.05 and 0.5C_{nom}, respectively, and the net discharge C-rate, including the rest periods between the consecutive elementary power profiles is $C_{nom}/3$. This value is to be compared with the 1C charge/discharge of the cell in the simple cycling mode. The total charge throughput during cycling is an alternative way of plotting capacity losses in different cycling conditions. Figure 5b compares capacity retentions of the cycle-aged cells as a function of the overall charge throughput. The corresponding capacity retentions as a function of time are reproduced in Fig. 5a for a better comparison. Figure 5b suggests that, at 45°C, the complex cycling is more damaging to the cell at a same charge throughput, whereas aging is almost insensitive to the cycling mode at 25°C. Interestingly, in our previous aging-simulation studies,[27,28] where cycle aging of a dummy graphite/$LiCoO_2$ cell was studied at 25°C, with a kinetic-limited growth of SEI layer at the graphite electrode as the only source of aging, the model predicted that the capacity loss depends on the charge throughput only, regardless of the C-rate value that is used. This modeling result, which additionally predicts nearly-linear capacity fade as a function of time, is in line with the experimental aging data under cycling at 25°C that are reported here and will be discussed in detail in a forthcoming report. Beside the lower average C-rate in the complex cycling mode, the rest periods are longer and more frequent in this mode of cycling as compared to the simple cycling. The fraction of total aging time that the cells spend at rest is about 30% for complex cycling, whereas it is only about 15% for the simple cycling. This result suggests the important role of storage aging at 45°C where it may dominate over the effect of charge throughput on the capacity loss of the cell.

Rate capability, impedance, and pulse test.—Figure 6 presents the charge/discharge rate capability of the cells obtained during intermediate characterization periods at 25°C. As it was explained in the 'Experimental section', the rate-capability tests were performed at C-rates ranging from C/10 to 3C by galvanostatic charge/discharge of the cells between 2 and 3.6 V. In order to make sure that the cells come back to a fully charged and discharged state, a CCCV protocol was used on both charge and discharge (CV until $|I| <$ C/25), respectively. The rate capability of a cell is a measure of its ability to deliver the same capacity in a defined potential window irrespective of the C-rate used to cycle the cell. When the cell impedance increases, cutoff potentials are reached sooner and there would be a decline in the rate capability of the cell. So, any change in the current dependence of the polarization effects in the cell is expected to show up as a change in the slope of the rate-capability curves of Fig. 6. Since the rate-capability tests were done using current values that were corrected for the capacity loss of the cells, additional polarization effects induced by a possible loss of active material do not show up in the data of Fig. 6. However, the increase of cell resistance caused by, e.g., the growth of resistive films on the active particles, a decrease of the electrolyte and/or the solid-matrix conductivity of the composite electrodes, should manifest themselves in Fig. 6. The rate-capability curves in Fig. 6 are translating along the capacity axis over time and remain virtually parallel to each other. This observation suggests that there is a negligible change of the cell impedance, regardless of the aging conditions.

In Fig. 7a, the impedance spectrum of the pristine graphite/LFP cell at 25°C and SOC = 40% is represented. As it was explained in the 'Experimental' section, the impedance spectra of the cells at different SOCs (0, 20, 40, 60, 80, and 100%) were obtained during the intermediate characterization periods by perturbing the open- circuit potential with an AC sinusoidal potential of 5 mV amplitude at frequencies ranging from 200 kHz to 10 mHz. Lumped-parameter equivalent-circuit models are frequently used to describe the impedance response of electrochemical systems. However, it is not straightforward to relate the equivalent-circuit parameters to the fundamental properties of the system. Moreover, the analysis is

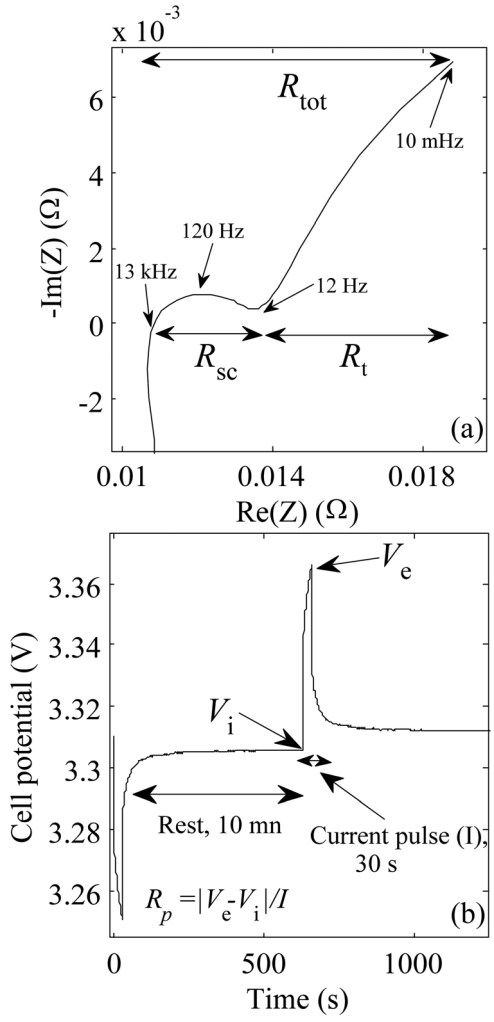

Figure 7. (a) AC impedance spectrum of the fresh graphite/LFP cell recorded at SOC = 40% and 25°C (b) potential profile of the fresh graphite/LFP cell subject to 30 s discharge and charge current-peaks at $1C_{nom}$ with 10 min rest in between (SOC = 40% and $T = 25°C$).

complicated because the impedance contains the contributions of both electrodes. So, here, we only provide a qualitative evaluation of the EIS spectra of the cells over aging. Figure 7a shows that the impedance spectrum of the graphite/LFP cell in the Nyquist plot representation is characterized by an inductive part at frequencies higher than ~13 kHz, a semicircle up to ~12 Hz and a nearly-linear tail at lower frequency. As a usual practice, the intercept of the impedance spectrum with the real axis at high frequencies is attributed to the electrolyte resistance, contact resistance between the porous electrode and current collector, and resistance of the external leads and connections. During the intermediate characterization periods, we had to disconnect the cells and take them out from the cell holders; hence, because of possible changes in cell-connection resistance, we discard the high-frequency part of the impedance spectra in the analysis. All the recorded spectra were shifted horizontally towards the origin of the Nyquist plot so that the qualitative comparison of the spectra over aging can be performed. Three types of resistance contributions were defined from the Nyquist plot of the cell in Fig. 7a: Semicircle resistance (R_{sc}), tail resistance (R_t), and total resistance (R_{tot}) which is the sum of semicircle and tail resistances. R_{sc} corresponds to the high and intermediate frequency ranges where fast processes like interfacial phenomena (e.g., charge-transfer kinetics) are dominant whereas R_t is dominated by transport limitations such as solid-state diffusion. The relative evolutions of these three resistances at SOC = 40% over aging time are represented in Fig. 8 for all aging conditions. Resistance values corresponding to the cells cycled or OCP-stored at 25°C remain nearly constant over the aging period whereas a clear increase in resistance is observed for all the cells aged at 45°C. As it is shown in Figs. 8d–8f, R_{sc}, R_t, and R_{tot} increase in a similar manner and almost by the same factor. The simultaneous and similar increase of R_{sc} and R_t could be interpreted as a consequence of active-material loss that in turn increases the cell impedance proportionally over the entire frequency range. This interpretation is in line with the analysis of the rate-capability curves above, which are based on C-rates corrected for capacity fade. A careful attention to the first few months of aging in Fig. 8 reveals that there is a slight decrease of the cell impedance. Transport limitations in the LFP electrode are significant because of the low value of diffusion coefficient, especially towards large values of y in Li_yFePO_4, and this result was confirmed in Ref. 29 for the same LFP electrodes as those in the cells studied here. If aging drives the cell in a stoichiometry window where y_{max} is decreased, one would expect smaller impedance values. Such an aging scenario is depicted in Fig. 2b where y_{max} is decreased because of the loss of cyclable lithium. This aging scenario will be confirmed in the following section. It should be noted that similar results were obtained at other SOCs and are not presented here.

The current-pulse test consists of discharge/charge current peaks at 1, 2, and $4C_{nom}$ and at different SOCs (20, 40, 60, and 80%). The peak duration is 30 s and there is 10 min rest between every consecutive discharge and charge peaks. Figure 7b shows the variation of the cell potential with time during the current-pulse test of the pristine cell at 25°C and SOC = 40% with $1C_{nom}$ discharge/charge peaks. We can define a resistance (R_p) based on the potential deviation ($V_e - V_i$) of the cell from its value before applying the current peak. R_p is defined as $(V_e - V_i)/I$ and has been monitored over aging for all the cells and at different SOCs. The variation of R_p at SOC = 40% derived from $1C_{nom}$ current peaks is represented in Fig. 9 for all the aging conditions. R_p varies with a similar trend as that observed for the impedance contributions of the cell in Fig. 8, but values are more scattered, possibly because high-frequency contributions, disregarded in the impedance analysis, are embedded in the values of R_p. Just like for impedance data, there is an overall increase of R_p at 45°C while there is no meaningful variation for the cells aged at 25°C. Similar results were obtained for R_p derived from 2 and $4C_{nom}$ current peaks and at other SOCs (20, 60, and 80%).

Rate-capability, impedance-spectroscopy, and pulse-test results show that there is a minor variation of the cell resistance after a year of aging. The maximum resistance increase of less than 60% observed for the graphite/LFP cell (Fig. 8) after a year of aging is lower than the impedance rise of other commercial cells even after shorter aging times in similar conditions.[30] Moreover, the homothetic increase of the cell impedance (except during the first few months) together with the constancy of the rate capability of the cells over aging suggests that the impedance rise is dominated by the loss of active material and not by an interfacial resistance increase of the electrodes.

Differential-voltage and differential-capacity analysis.—The advantages of differential-voltage and differential-capacity analyses in the aging study of the graphite/LFP cell were discussed in the'Aging-analysis framework' section. Here, we analyze the aging of the cells with the aid of these two methods. The differential-capacity curves are obtained from PITT measurements that were carried out during the intermediate characterization periods. The charge passed at each 10 mV increment provides us with a direct evaluation of the differential capacity. Figures 10c and 10d represent the evolution of the $V - d|Q|/dV$ curves corresponding to the cells aged under simple cycling at 25 and 45°C, respectively, derived from PITT data on discharge. The differential-voltage curves were derived from the

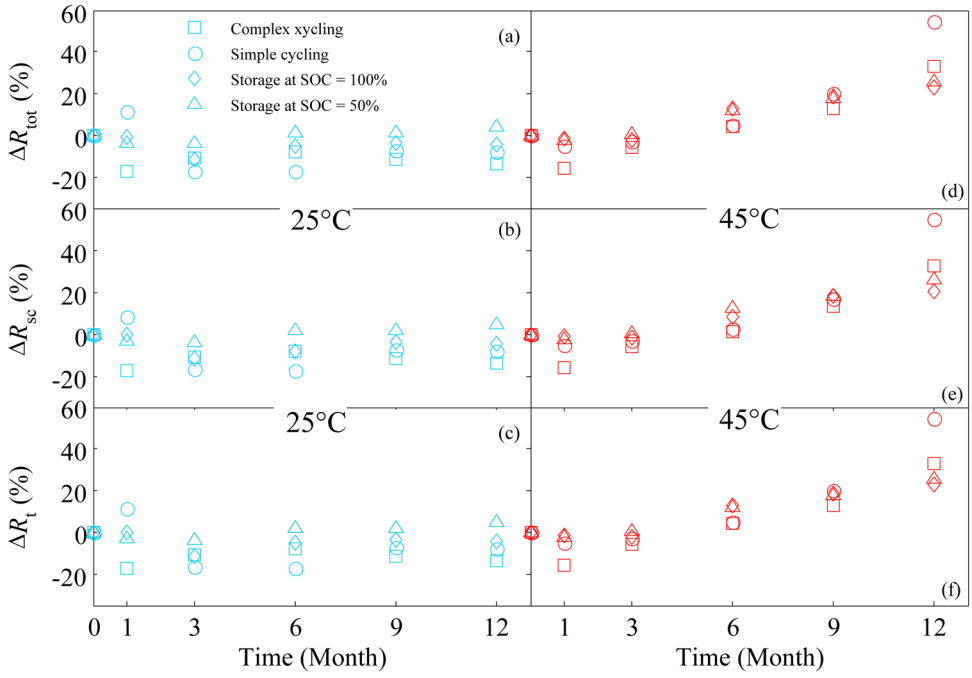

Figure 8. (Color online) Evolution of semicircle resistance (R_{sc}), tail resistance (R_t), and total resistance (R_{tot}) deduced from the impedance spectra of the graphite/LFP cells at SOC = 40% during the intermediate characterization periods. (a) to (c) cells aged at 25°C; (d) to (f) cells aged at 45°C.

galvanostatic C/10 discharge data recorded during the intermediate characterization periods. The cell potential was numerically differentiated with respect to a constant capacity increment (50 mAh) and the results are represented in Figs. 10a and 10b for simple cycling at 25 and 45°C, respectively. A comparison between the differential-voltage and differential-capacity curves of the graphite/LFP cell of Fig. 10 and those of the graphite electrode already presented in Fig. 3 reveals the qualitative similarity between the complete cell and the graphite electrode. In Fig. 10, the cell potential and capacity of the graphite/LFP cell have been divided in four regions, namely A, B, C, and D, in a similar manner as for the graphite electrode in the 'Aging-analysis framework' section.

For simple cycling at 25 and 45°C, there is a progressive decrease of the capacity of region D in the differential-voltage plots (Figs. 10a and 10b), in line with a progressive decrease of the magnitude of the corresponding peak at 3.33 V in the differential-capacity plots (Figs. 10c and 10d). For simple cyling at 45°C, this decrease is faster, and the capacity of this region (or peak) eventually goes to zero, unlike for the cycling at 25°C. The loss of cyclable lithium is at the origin of this aging behavior. Additionally, for the cycling at 45°C, there is also a decrease of the capacities of other regions (peaks) after about 6 months, which is indicative of active-material loss in the graphite electrode, as discussed in more detail in the following. Finally, there is virtually no change of the peak

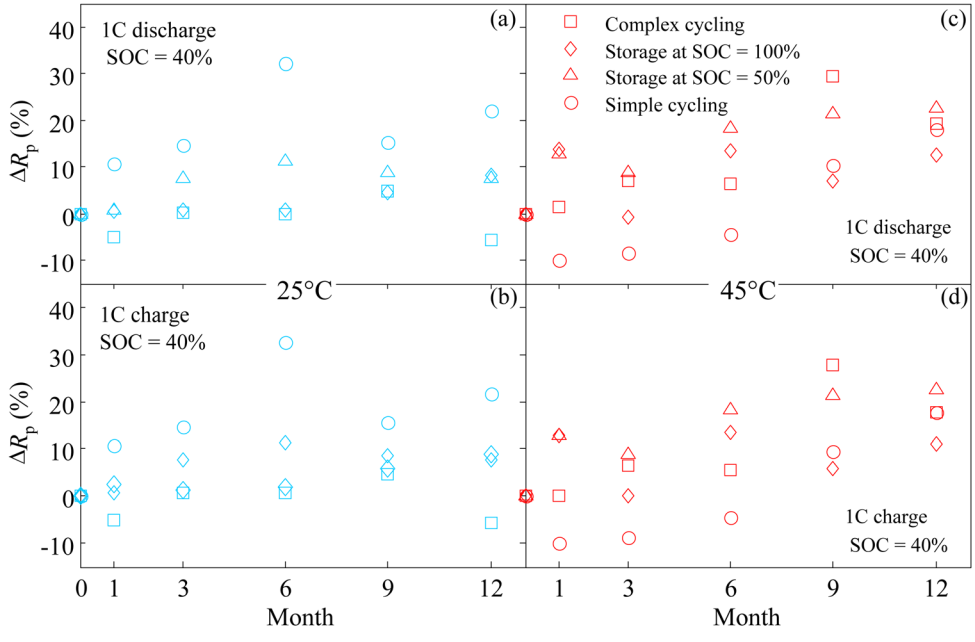

Figure 9. (Color online) Evolution of R_p resistance calculated from the pulse tests of the graphite/LFP cells at SOC = 40% and by applying $1C_{nom}$ (a) discharge current peak to the cells aged at 25°C (b) charge current peak to the cells aged at 25°C (c) discharge current peak to the cells aged at 45°C (d) charge current peak to the cells aged at 45°C.

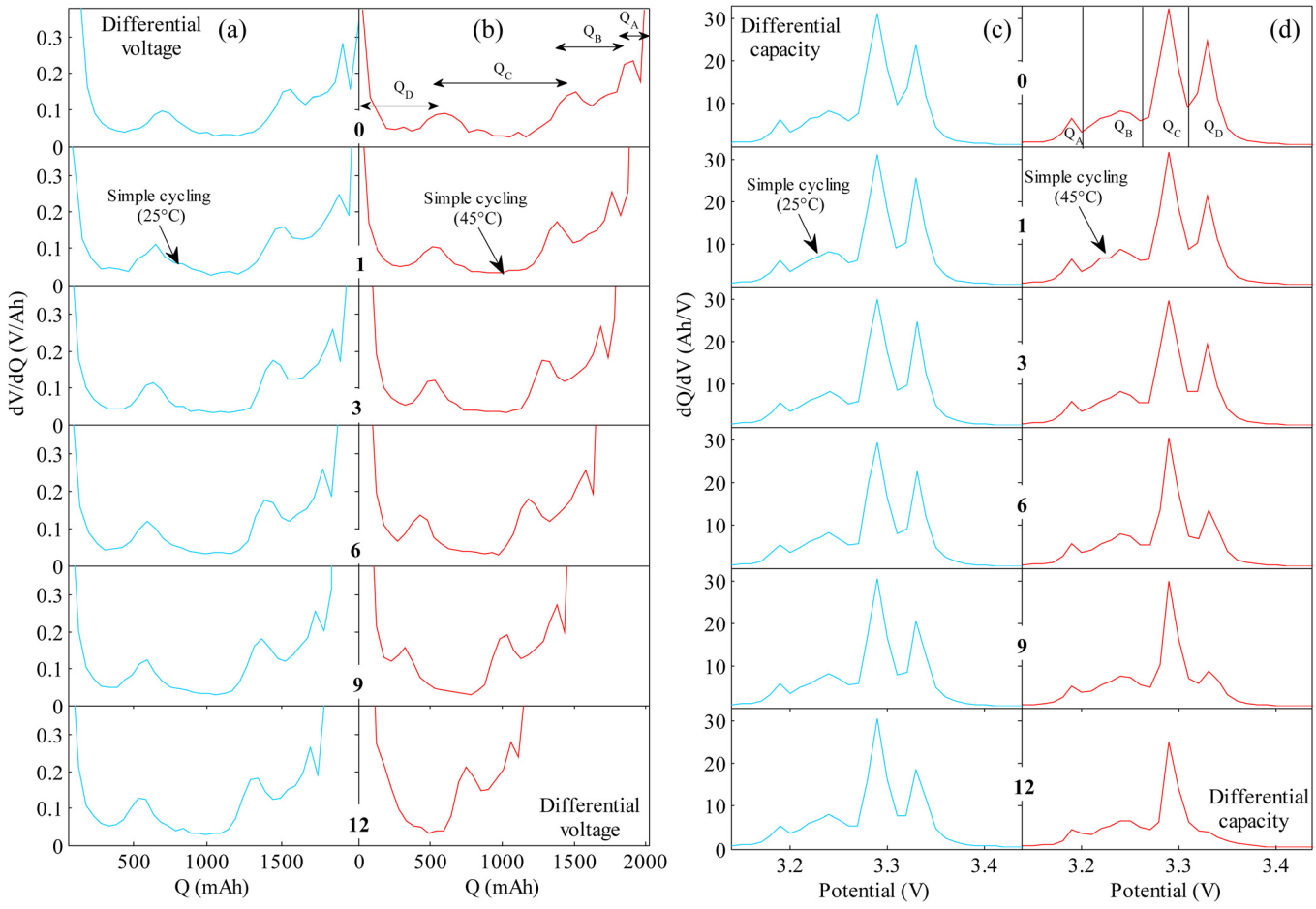

Figure 10. (Color online) Evolution of the (a), (b) differential-voltage and (c), (d) differential-capacity signatures of the graphite/LFP cells recorded during the intermediate characterization periods at 25°C for the cell aged over a year under (a), (c) simple cycling at 25°C or (b), (d) simple cycling at 45°C.

positions in Figs. 10c and 10d, which is another clue that there is a negligible change of the cell impedance.

The relative evolution of the cell capacities delivered in regions A, B, C, and D were calculated for all the aging conditions based on the capacities between the peaks in the differential-voltage curves similar to those of Fig. 10 and are represented in Figs. 11a–11d. The cell capacity in region D (Q_D) clearly decreases for all the aging conditions. Note that there are no markers at month #12 for Q_D for the cells under simple and complex cycling at 45°C in Fig. 11a, because the peak between regions C and D has vanished, which means that the contribution of the region D of the graphite electrode to the cell capacity is almost zero. The cells aged at 45°C experience a faster decrease of Q_D than those aged at 25°C, and among those cells, the fastest rate of decrease is for those under cycling conditions. For the cells aged at 25°C, the rate of decrease for those under cycling and those under storage is nearly equivalent.

The relative evolution of the cell capacity in region C (Q_C) is represented in Fig. 11b for all the aging conditions. Q_C slightly decreases for the cells aged at 45°C whereas no clear trend of decline is observed for the cells aged at 25°C. The disappearance of the peak between C and D regions in the differential-voltage plot and of the peak associated with Q_D in the differential-capacity plot does not necessarily mean that the graphite electrode no longer operates on region D; therefore, defining Q_C as the capacity between the "B-C" peak and the maximum capacity in the absence of the "C-D" peak is not proper, which is why there is no marker for Q_C at month #12 in Fig. 11b accordingly.

The relative values of cell capacities in region B (Q_B) and A (Q_A) are represented in Figs. 11c and 11d, respectively. The variations of Q_B and Q_A are highly scattered for all the cells. Therefore, they are not taken into account for the aging analysis. However, the clear decrease of Q_D for all aging conditions and the slight decline of Q_C for the cells aged at 45°C provide useful information regarding the source of capacity loss of the graphite/LFP cells. The cells can be studied into two main groups. The first group contains the cells aged at 25°C and the second group consists of the cells aged at 45°C. The aging of the cells of the first group is solely characterized by a continuous decrease of Q_D over time. The contribution of the region D of the graphite electrode to the cell capacity becomes less and less whereas other regions deliver about the same capacity as initially. A continuous loss of cyclable lithium (Fig. 2b) can account for the capacity loss observed for the cells of this first group. The gradual depletion of cyclable lithium shortens the operating stoichiometry window of the graphite electrode in a way that its higher stoichiometry is shifted towards lower values of x_{max} (Fig. 2b). In the second group, the situation is similar to that of the first group during the first 6 months of aging where the cyclable lithium loss is a dominant contribution to the cell aging. However, after 6 months, Q_C starts decreasing while the region D still accounts for part of the cell capacity, which is in line with a gradual loss of graphite active material in the cell as an additional source of aging (Fig. 2d).

OCP Storage.—As it was explained in the 'Experimental' section, the intermediate characterization tests for the cells under storage starts with three discharge/charge cycles composed of a galvanostatic discharge (charge) up to 2 (3.6) V followed by a constant voltage until $|I| < C_{nom}/25$. let us denote the CCCV discharge capacity of the cell after storage $Q_{1,i}$ and $Q_{3,i}$ for the first and third discharges

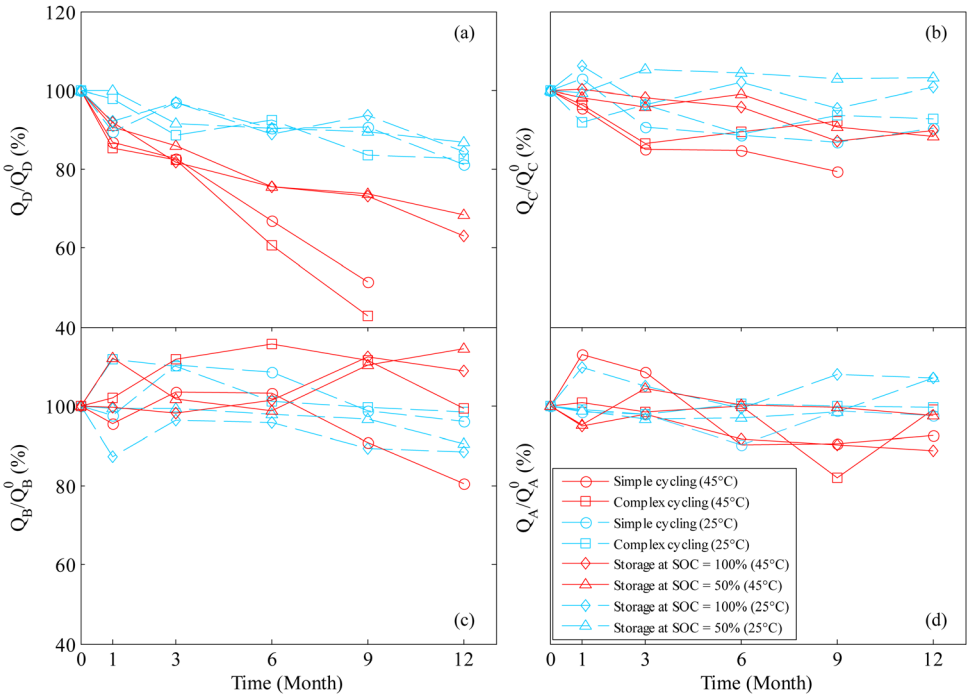

Figure 11. (Color online) Evolution of the cell capacities delivered in different stoichiometry regions of the graphite/LFP cell relative to the corresponding capacities before aging, for all the aging conditions calculated from the peak distances in the differential-voltage signature graphs of the cells recorded during the intermediate characterization periods at 25°C (a) relative capacity in region D (Q_D/Q_D^0) (b) relative capacity in region C (Q_C/Q_C^0) (c) relative capacity in region B (Q_B/Q_B^0) (d) relative capacity in region A (Q_A/Q_A^0).

of the cell at characterization # i, respectively. With this notation, $Q_{3,i-1}$ stands for the third-discharge capacity of the cell at intermediate characterization # i -1. Three types of capacity loss are defined

$$\Delta Q_{\text{app},i} = \left\{ \begin{array}{l} Q_{3,i-1} - Q_{1,i}, \text{for the two cells stored at SOC} = 100\% \\ \dfrac{Q_{3,i-1}}{2} - Q_{1,i}, \text{for the two cells stored at SOC} = 50\% \end{array} \right\}$$

$$\Delta Q_{\text{irr},i} = Q_{3,i-1} - Q_{3,i}$$

$$\Delta Q_{\text{rev},i} = \Delta Q_{\text{app},i} - \Delta Q_{\text{irr},i}$$

where $\Delta Q_{\text{app},i}$, $\Delta Q_{\text{irr},i}$, and $\Delta Q_{\text{rev},i}$ stand for apparent (or total), irreversible, and reversible capacity losses arising from cell storage in OCP conditions between two consecutive intermediate characterizations, respectively. These three types of loss are calculated for the cells under storage conditions and are represented in Fig. 12. Note

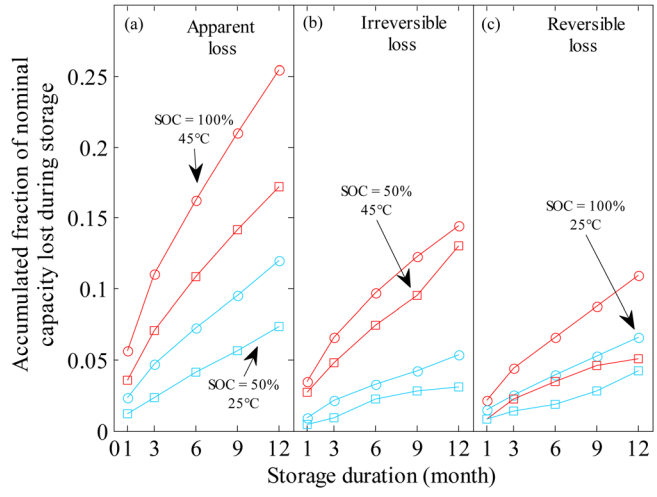

Figure 12. (Color online) Accumulated (a) Apparent, (b) irreversible, and (c) reversible loss of capacity during the OCP storage of the graphite/LFP cells at SOCs of 50 and 100% and at storage temperatures of 25 and 45°C, measured during the intermediate characterization periods at 25°C.

that each type of capacity loss is accumulated over the overall storage time and is normalized to the nominal capacity of the cell. For all the four storage conditions presented in Fig. 12, there is part of the capacity loss that is recovered in the subsequent cycles following the first immediate discharge of the cell (i.e., reversible loss). Irreversible and reversible capacity losses are of the same order of magnitude and amount to a few percents of the nominal capacity of the cell per month of storage (Fig. 12). Whereas irreversible and reversible losses are very similar at 25°C, irreversible losses exceed reversible ones at 45°C. The influence of temperature and SOC on irreversible losses is qualitatively similar to that of apparent losses. However, the temperature has less effect than the SOC on reversible losses (compare the curves at 25°C and SOC = 100% and at 45°C and SOC = 50%).

Reversible capacity loss is experienced by all Li-ion systems.[31] The high potential of Li-ion batteries especially at a completely charged state, makes it more likely for the lithiated graphite negative and delithiated positive electrode to be oxidized or reduced by the electrolyte, respectively.[32] There is no detailed study of the OCP-storage aging of the graphite/LFP cell in the literature; However, the loss of cyclable lithium because of side reactions at the graphite electrode has been reported as the main source of aging in other Li-ion batteries with a carbonaceous anode.[31] The reversible loss of capacity during OCP storage arises from side reactions occurring at the anode and cathode electrodes simultaneously with equal amounts of cyclable-lithium ions exchanged between the electrodes and electrolyte at both electrode. Usually, a same species is involved at both electrodes, acting as a shuttle.[31] The reaction of acidic impurities generated at the cathode with the SEI is an example of shuttle mechanism.[33–35] Sloop et al.[34] proposed a shuttle mechanism that is worth being noted here. $LiPF_6$ acts as a Lewis acid with EC-containing electrolytes to generate transesterification products, PEO polymers and CO_2. CO_2 is easily reduced at the anode to oxalate or CO. The oxalate is sufficiently soluble to reach the cathode where it is reoxidized back to CO_2 thus resulting in a shuttle mechanism.

As explained in the "Experimental" section, the OCP of the stored cells was recorded every 15 days during the storage period. Figure 13 shows the OCP decrease of the cells under different

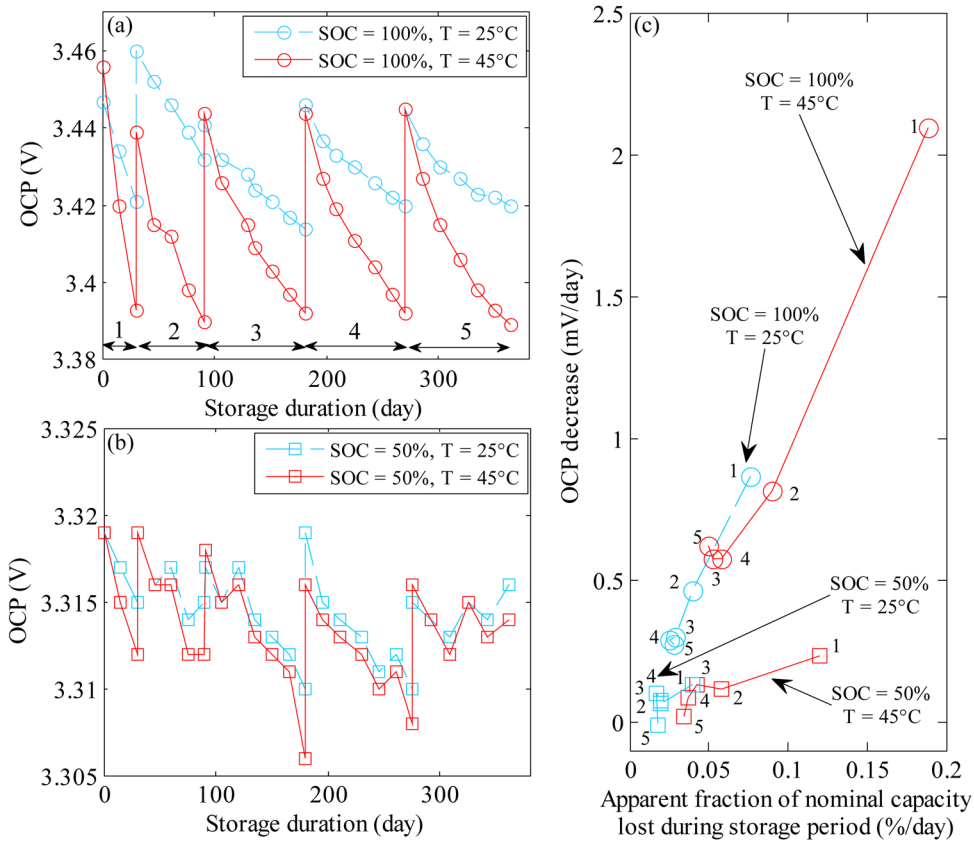

Figure 13. (Color online) OCP of the graphite/LFP cells during the storage conditions at 25 and 45°C and (a) SOC = 100% (b) SOC = 50%. (c) Rate of OCP decrease of the cells stored under different aging conditions as a function of the corresponding rate of apparent (or total) capacity loss (expressed in fraction of the nominal capacity).

storage conditions. The potential decrease is substantial and well-defined for the cells stored at SOC = 100% (Fig. 13a) whereas the cells stored at SOC = 50% experience subtle variations of potential only (Fig. 13b). At SOC = 50%, both electrode compositions are such that electrode potentials are flat or nearly flat (Fig. 2a). The cell-potential decrease is a direct consequence of side reactions during the cell storage. Different scenarios could make the cell potential decrease during storage: Lithium uptake by the LFP electrode, lithium release by the graphite electrode, or both at the same time. In Fig. 13c the average rate of decrease of the cell potential of the OCP-stored cells between two consecutive intermediate characterizations is represented as a function of their corresponding average rate of apparent capacity loss. Regardless of the storage conditions, the rate of capacity loss and OCP decrease are the highest during the first month of storage. Moreover, the rate of OCP decrease declines almost linearly with that of capacity loss up to 6 months of storage for all the conditions but storage at 25°C and SOC = 50%. The rate of OCP decrease and capacity loss stabilize after 6 months of storage at SOC = 100% for both 25 and 45°C conditions. For the cells stored at SOC = 50%, there is no obvious trend between the rate of OCP decrease and that of capacity loss after 6 months of storage at 25°C. As for the cells stored at 45°C more than 6 months, the rate of capacity loss remains almost constant although the rate of OCP-decrease slightly declines.

Given the extent of potential decrease between two consecutive intermediate characterization periods for the case of aging tests at SOC = 100% and the graphite electrode OCP that is almost flat near SOC = 100%, there is a definite contribution of the LFP electrode on the OCP decrease of the cell, which explains why a reversible capacity loss is measured in storage conditions. Indeed, the OCP of the LFP electrode at a completely charged state of the cell is very sensitive to small variations of lithium content and substantially contributes to the OCP decrease of the cells even though it involves only minor uptake of lithium ions resulting from a side reaction. Hence, the contribution of both electrodes in the aging under storage condition is clearly demonstrated. A side reaction at the charged LFP electrode partially compensates for the lithium release at the graphite electrode (i.e., because of the side reaction leading to SEI growth at the anode).

Cycling.—As detailed in the "experimental section," the performance of the graphite/LFP cell under cycling was examined by using two modes of cycling, namely simple and complex modes, at 25 and 45°C. The simple cycling consists of continuous galvanostatic charge/discharge of the cell between 2 and 3.6 V with 10 min rest between each charging or discharging segments. In the complex cycling mode, the cell is first charged at $C_{nom}/2$ up to 3.6 V. The cell is then left at rest for 30 min and then is discharged down to 3 V by the repetition of 985 s power profiles, each of them being followed by a 10 min rest period (Figs. 1b and 1c). The discharge capacities of the cells for the two modes of cycling at 25 and 45°C as a function of cycle number are represented in Figs. 14a and 14b, respectively. Discharge capacities measured with a CCCV protocol (C/10 and CV until $|I| < C/25$) at 25°C during the intermediate characterization periods are also added to the figure, and are represented by markers. As for the simple cycling, capacities recorded during cycling are lower than those measured during the characterization periods; the difference between the two is nearly constant over cycle number, and substantially larger for the simple cycling at 25°C. These differences in capacities are explained by polarization effects of the $1C_{nom}$ cycling profile, compared with the low rate (C/10) measurement used during the characterizations. The difference is less for the cycling at 45°C because of the lower polarization at higher temperature that partially counterbalances the rate effect.

For the cells under complex cycling (Fig. 14b), the cell capacity during the discharge periods of the complex profile (solid and dotted lines) and the measured cell capacity during the intermediate characterization periods (circle and square markers) are very close to each other both at 25 and 45°C, as a consequence of the average C-rate ($C_{nom}/3$ on discharge and $C_{nom}/2$ on charge) which is closer to

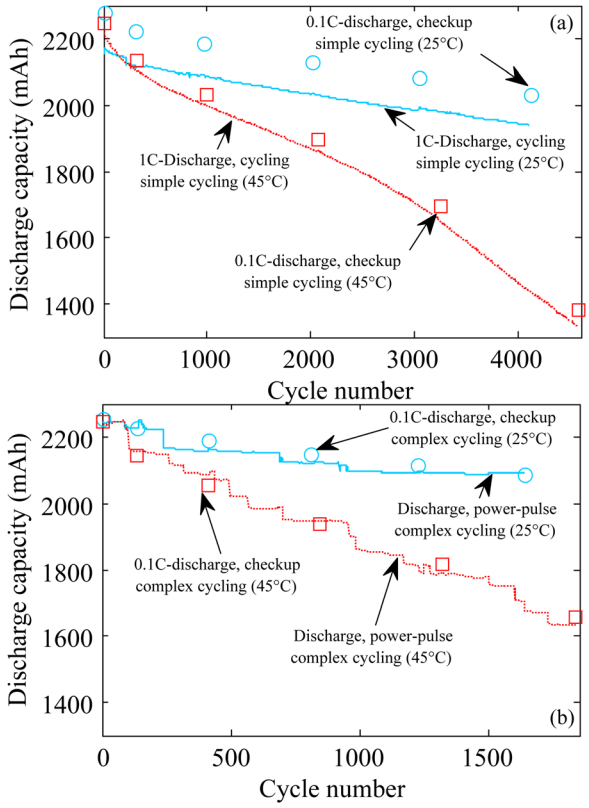

Figure 14. (Color online) Discharge capacity of the cells a function of cycle number (solid and dotted lines) along with the low-rate capacities measured during the intermediate characterization periods at 25°C (circle markers for the cells cycled at 25°C and square markers for the cells cycled at 45°C) for (a) simple cycling at 25°C (solid line) and 45°C (dotted line) (b) complex cycling at 25°C (solid line) and 45°C (dotted line).

that used during characterizations. Here, contrary to the simple cycling mode where the capacity decreases smoothly over cycling, the capacity loss is stepwise because of the premature end of discharge caused by the intense power peak at 750 s (Fig. 1). The similar trends of cell capacities measured during cycling and intermediate

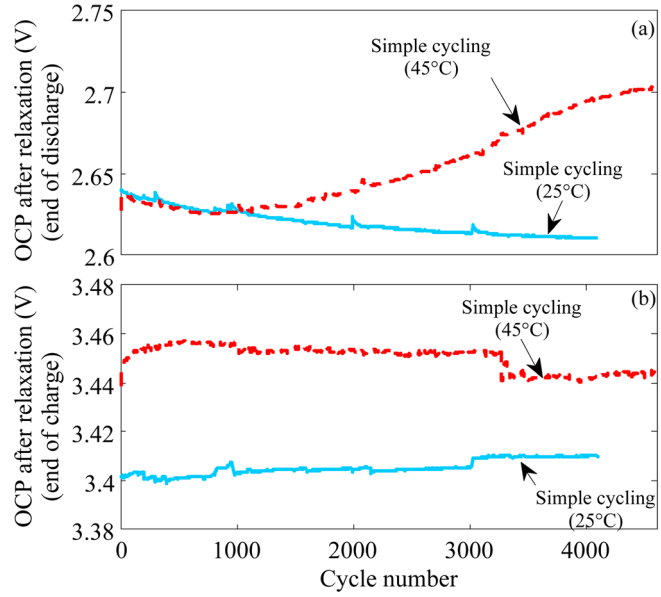

Figure 15. (Color online) Cell potential at the end of 10 min relaxation periods following the (a) $1C_{nom}$ discharge and (b) $1C_{nom}$ charge cycles during the simple cycling modes at 25 (solid lines) and 45°C (dotted lines).

characterization periods in Fig. 14 are another proof for the minor increase of the cell resistance over aging.

The cell potential at the end of the relaxation periods following the $1C_{nom}$ charge and discharge cycles of the simple cycling mode are represented in Figs. 15a and 15b, respectively. The potential values are assumed close to the equilibrium values after 10 min of rest. There are minor variations of OCP values at the end of charge, regardless of the cycling temperature (Fig. 15b). As already discussed in the 'Differential-capacity and differential-voltage analysis' section, the graphite electrode at the end of charge remains in region D for the overall aging period at 25°C and up to about 9 months for the cycling at 45°C; therefore it is nearly unchanged. As a consequence, the nearly-stable end-of-charge OCP values over cycling suggest that the LFP electrode does not experience a major resistance increase, in which case a decrease of the end-of-charge

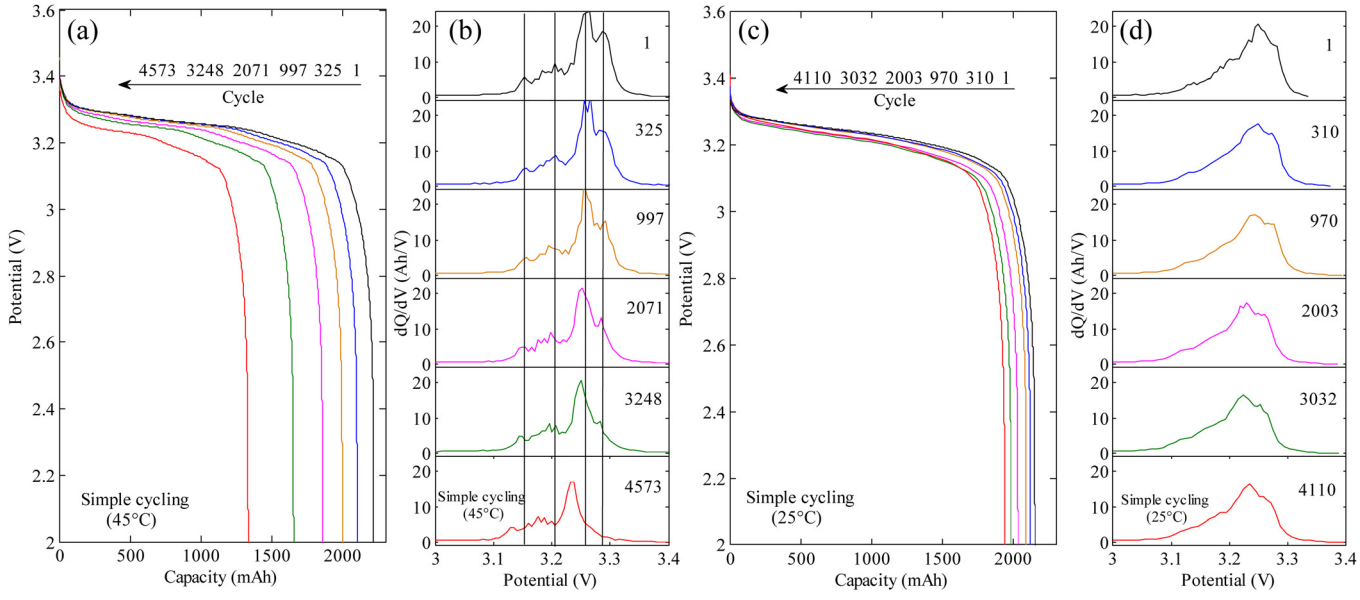

Figure 16. (Color online) Selected $1C_{nom}$ discharge cycles of the graphite/LFP cells during (a) simple cycling at 25°C and (c) simple cycling at 45°C along with their corresponding differential-capacity signature graphs; (b) simple cycling at 25°C (d) simple cycling at 45°C.

potential would result. The OCP of the cells at the end-of-discharge, however, show clear trends of variation over cycling (Fig. 15a). There is a monotonic decrease of the OCP at 25°C (solid line) whereas the OCP first decreases during the first 1000 cycles and then goes up during the subsequent cycles at 45°C (dotted line). As proposed in the 'Rate-capability, impedance, and pulse tests' section, the loss of cyclable lithium slowly drives the cell into a stoichiometry window where the LFP has a better rate capability (Fig. 2c). The lower polarization of the LFP electrode leaves a larger margin of potential rise for the graphite electrode before the cell reaches the cutoff potential during discharge, which translates into a lower value of x_{min}. This is in line with the gradual decrease of OCP at the end of discharge for the simple cycling at 25°C (solid line in Fig. 15a) where the loss of cyclable lithium was shown to be the dominant source of capacity loss over the whole aging period in the 'Differential-capacity and differential-voltage analysis' section. The initial OCP decrease at the end of discharge for simple cycling at 45°C is induced by a similar improvement of the rate capability of the LFP electrode because of cyclable lithium loss. The loss of graphite active material after 1000 cycles leads to a gradual rise of polarization of the graphite electrode at which the superficial current density keeps on increasing along with the decrease of its active surface area. Hence, the graphite electrode is less and less deintercalated by the end of cell discharge and this results in an increase of the OCP (dotted line in Fig. 15a). In Fig. 16, some selected discharge cycles along with their corresponding differential-capacity signatures are presented for the simple cycling conditions at 25 and 45°C. At 45°C, the polarization is almost constant up to 997 cycles. After that, there is more and more polarization showing up as clearly outlined by the peak shift towards the left hand side in the differential-capacity signature plots of Fig. 16b. This result is in line with the impedance increase caused by the decrease of active-surface area of the graphite electrode arising from the active-material loss, as discussed above. It is noteworthy that the polarization increase shows up because the cycling is performed under a nominal C-rate ($1C_{nom}$), kept constant over cycling. Such a polarization increase is not visible in the rate-capability tests performed during the intermediate characterization periods (Fig. 6), where current densities were corrected for capacity loss. At 25°C, although the peaks in the differential-capacity signature graphs are broader (Fig. 16d) due to the polarization that is larger at 25°C than at 45°C, we can see that there is virtually no peak shift upon cycling that supports the absence of active-material loss in this cycling condition.

Conclusion

The results of a 1-year aging study of the commercial 2.3 Ah graphite/LFP cell under 8 different cycling or storage conditions at either 25 or 45°C was presented. The comparison of the cells aged at a same temperature revealed that the cells under cycling lose more capacity than those under OCP storage. Aging was shown to be very sensitive to the temperature at which the cells were aged; the capacity loss was up to four times larger for cells aged at 45°C under the same cycling conditions. The qualitative similarity between the complete cell and the graphite electrode differential-capacity and differential-voltage signatures allowed for the utilization window of the cells to be tracked over the aging period. These analyses confirmed that capacity fade is dominated by the loss of cyclable lithium for all aging conditions, along with a slight loss of graphite active material near the end of the aging period for cycling conditions at 45°C. These results were qualitatively confirmed by the evolution of the end-of-discharge potentials of the cells under cycling conditions. Rate-capability, impedance spectroscopy, and current-pulse tests revealed a minor increase of the cell impedance for experiments at 45°C and virtually no change for those at 25°C. The impedance increase at 45°C likely arises from the graphite active-material loss that results in a decrease of the active surface area of the anode.

The capacity decrease of the cells over aging exhibits a linear trend except during the first few months and there is an acceleration after 6 months for the cells aged under cycling at 45°C that probably arises from the graphite active-material loss at this temperature. The comparison of capacity losses of the cells subject to a conventional galvanostatic charge/discharge at $1C_{nom}$ and a complex power-current profile with an average discharge rate of $C_{nom}/3$ and a charge rate of $C_{nom}/2$ provided interesting results. Whereas the capacity loss as a function of time was always larger for the $1C_{nom}$ cycling regardless of the temperature, the two cycling profiles at 25°C yielded similar capacity losses when plotted against the total charge throughput. This result, along with the nearly linear trend of capacity decline suggests that the loss of cyclable lithium might be governed by a kinetic-limited growth of the SEI layer at the graphite electrode based on our previous aging modeling studies. For cycling at 45°C, the complex cycling profile was more detrimental than the conventional cycling in terms of capacity fade when plotted against the charge throughput, which suggests a strong impact of the rest periods on the cell aging at such a temperature. Aging of the cells under OCP-storage conditions was featured with both irreversible and reversible capacity losses, both amounting to a few percents of the nominal capacity of the cell per month of storage. Moreover, the contribution of both electrodes in the aging under storage condition was clearly demonstrated through an analysis of OCP decrease and capacity loss during the storage periods; A side reaction at the charged LFP electrode partially compensates for the lithium release at the graphite electrode (i.e., because of the side reaction leading to SEI growth at the anode), thus accounting for a reversible capacity loss.

The following papers will report on the postmortem analyses and aging modeling of the cells presented in this work in order to confirm the aging hypotheses that were proposed in this study.

Acknowledgments

M. S. and C. D. are grateful to M. Morcrette, A. Teyssot, C. Dudzert, and P. Gyan for helpful discussion.

References

1. A. K. Padhi, K. S. Nanjundaswamy, and J. B. Goodenough, *J. Electrochem. Soc.*, **144**, 1188 (1997).
2. http://www.uscar.org/guest/publications, last accessed May 2011.
3. K. Striebel, A. Guerfi, J. Shim, M. Armand, M. Gauthier, and K. Zaghib, *J. Power Sources*, **119–121**, 951 (2003).
4. J. Shim and K. A. Striebel *J. Power Sources*, **119–121**, 955 (2003).
5. K. Zaghib, K. Striebel, A. Guerfi, J. Shim, M. Armand, and M. Gauthier, *Electrochim. Acta*, **50**, 263 (2004).
6. K. Striebel, J. Shim, A. Sierra, H. Yang, X. Song, R. Kostecki, and K. McCarthy, *J. Power Sources*, **146**, 33 (2005).
7. K. Amine, J. Liu, and I. Belharouak, *Electrochem. Commun.*, **7**, 669 (2005).
8. K. Zaghib, N. Ravet, M. Gauthier, F. Gendron, A. Mauger, J.B. Goodenough, and C. M. Julien, *J. Power Sources*, **163**, 560 (2006).
9. M. Koltypin, D. Aurbach, L. Nazar, and B. Ellis, *Electrochem. Solid-State Lett.*, **10**, A40 (2007).
10. M. Koltypin, D. Aurbach, L. Nazar, and B. Ellis, *J. Power Sources*, **174**, 1241 (2007).
11. M. Dubarry and B. Y. Liaw, *J. Power Sources*, **194**, 541 (2009).
12. P. Liu, J. Wang, J. Hicks-Garner, E. Sherman, S. Soukiazian, M. Verbrugge, H. Tataria, J. Musser, and P. Finamore, *J. Electrochem. Soc.*, **157**, A499 (2010).
13. J. Wang, P. Liu, J. Hicks-Garner, E. Sherman, S. Soukiazian, M. Verbrugge, H. Tataria, J. Musser, and P. Finamore, *J. Power Sources*, **196**, 3942 (2011).
14. M. Dubarry, B. Y. Liaw, Mao-Sung Chen, S.-S. Chyan, K.-C. Han, W.-T. Sie, and S.-H. Wu, *J. Power Sources*, **196**, 3420 (2011).
15. S. B. Peterson, J. Apt, and J. F. Whitacre, *J. Power Sources*, **195**, 2385 (2010).
16. P. Arora, R. E. White, and M. Doyle, *J. Electrochem. Soc.*, **145**, 3647 (1998).
17. J. Vetter, P. Novák, M. R. Wagner, C. Veit, K.-C. Mller, J. O. Besenhard, M. Winter, M. Wohlfahrt-Mehrens, C. Vogler, and A. Hammouche, *J. Power Sources*, **147**, 269 (2005).
18. J. Christensen and J. Newman, *J. Electrochem. Soc.*, **152**, A818 (2005).
19. J. Christensen and J. Newman, *J. Electrochem. Soc.*, **150**, A1416 (2003).
20. M. Safari and C. Delacourt, *J. Electrochem. Soc.*, **158**, A562 (2011).
21. Q. Zhang and R. E. White, *J. Power Sources*, **179**, 793 (2008).
22. A. H. Thompson, *J. Electrochem. Soc.*, **126**, 608 (1979).
23. I. Bloom, A. N. Jansen, D. 1 P. Abraham, J. Knuth, S. A. Jones, V. S. Battaglia, and G. L. Henriksen, *J. Power Sources*, **139**, 295 (2005).
24. I. Bloom, J. Christophersen, and K. Gering, *J. Power Sources*, **139**, 304 (2005).

25. M. Dubarry, V. Svoboda, R. Hwu, and B. Y. Liaw, *Electrochem. Solid-State Lett.*, **9**, A454 (2006).
26. T. Ohzuku, Y. Iwakoshi, and K. Sawai, *J. Electrochem. Soc.*, **140**, 2490 (1993).
27. M. Safari, M. Morcrette, A. Teyssot, and C. Delacourt, *J. Electrochem. Soc.*, **157**, A713 (2010).
28. M. Safari, M. Morcrette, A. Teyssot, and C. Delacourt, *J. Electrochem. Soc.*, **157**, A892 (2010).
29. M. Safari and C. Delacourt, *J. Electrochem. Soc.*, **158**, A63 (2011).
30. P. Ramadass, B. Haran, R. White, and B. N. Popov, *J. Power Sources*, **111**, 210 (2002).
31. M. Broussely, S. Herreyre, P. Biensan, P. Kasztejna, K. Nechev, and R. J. Staniewicz, *J. Power Sources*, **97–98**, 13 (2001).
32. Y. Ozawa, R. Yazami, and B. Fultz, *J. Power Sources*, **119–121**, 918 (2003).
33. E. Wang, D. Ofer, W. Bowden, N. Iltchev, R. Moses, and K. Brandt, *J. Electrochem. Soc.*, **147**, 4023 (2000).
34. S. E. Sloop, J. B. Kerr, and K. Kinoshita, *J. Power Sources*, **119–121**, 330 (2003).
35. R. Spotnitz, *J. Power Sources*, **113**, 72 (2003).